(De)Lithiation Mechanism of Li/SeSₓ (x = 0−7) Batteries Determined by in Situ Synchrotron X-ray Diffraction and X-ray Absorption Spectroscopy

Yanjie Cui,[†] Ali Abouimrane,*[,†] Jun Lu,[†] Trudy Bolin,[‡] Yang Ren,[‡] Wei Weng,[†] Chengjun Sun,[‡] Victor A. Maroni,[†] Steve M. Heald,[‡] and Khalil Amine[†,§]

[†]Chemical Science and Engineering Division and [‡]X-ray Science Division, Argonne National Laboratory, Argonne, Illinois 60439, United States

[§]King Abdulaziz University, Jeddah, Saudi Arabia

S *Supporting Information*

ABSTRACT: Electrical energy storage for transportation has gone beyond the limit of converntional lithium ion batteries currently. New material or new battery system development is an alternative approach to achieve the goal of new high-energy storage system with energy densities 5 times or more greater. A series of SeS_x−carbon ($x = 0-7$) composite materials has been prepared and evaluated as the positive electrodes in secondary lithium cells with ether-based electrolyte. In situ synchrotron high-energy X-ray diffraction was utilized to investigate the crystalline phase transition during cell cycling. Complementary, in situ Se K-edge X-ray absorption near edge structure analysis was used to track the evolution of the Se valence state for both crystalline and noncrystalline phases, including amorphous and electrolyte-dissolved phases in the (de)lithiation process. On the basis of these results, a mechanism for the (de)lithiation process is proposed, where Se is reduced to the polyselenides, Li_2Se_n ($n \geq 4$), Li_2Se_2, and Li_2Se sequentially during the lithiation and Li_2Se is oxidized to Se through Li_2Se_n ($n \geq 4$) during the delithiation. In addition, X-ray photoelectron spectroscopy and electrochemical impedance spectroscopy demonstrated the reversibility of the Li/Se system in ether-based electrolyte and the presence of side products in the carbonate-based electrolytes. For Li/SeS_2 and Li/SeS_7 cells, Li_2Se and Li_2S are the discharged products with the presence of Se only as the crystalline phase in the end of charge.
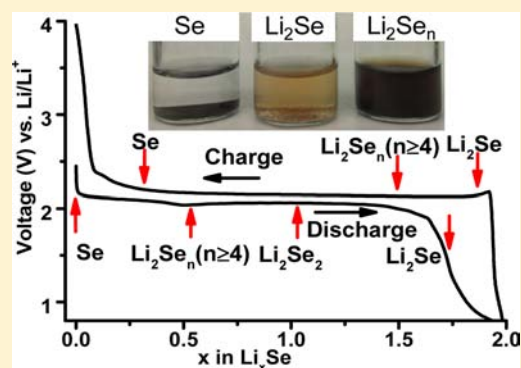
1. INTRODUCTION

The desire for effective utilization of renewable resources, including solar, tidal, and wind, for transportation applications as a replacement for fossil fuels and the widespread use of portable electronics has created great opportunities for development of new energy storage systems. State-of-the-art rechargeable batteries are mainly based on conventional lithium intercalation chemistry, using lithium transition metal oxides as cathode material with typical capacities of 120−160 mA·h/g.[1,2] The low energy density and/or high cost of these cathode materials have limited their large-scale production and application in Li ion batteries. Discovery of new cathode materials with higher energy density is, thus, a key to realizing more efficient energy storage systems. Recently, lithium−sulfur (Li/S)[3−5] and lithium−oxygen (Li/O₂) cells[6−9] have been demonstrated to possess the potential to provide 2−5 times the energy density of conventional Li ion cells. However, both Li/S and Li/O₂ cells suffer from poor cycling performance, which had impeded their commercial utilization. For instance, the cyclability of Li/O₂ cells is limited by severe electrolyte decomposition and large cell polarization under deep discharge/charge conditions,[10,11] while Li/S cells suffer from

the solubility of intermediate lithium polysulfide species during cycling, which causes the so-called redox shuttle effect and, thus, poor cyclability.[12−14]

In a previous paper, we demonstrated the potential of a new class of rechargeable lithium and sodium batteries based on selenium as the active cathode material.[15] The choice of selenium, which is a d-electron-containing member of group 16 in the periodic table, is due to its higher electrical conductivity compared to sulfur and high theoretical gravimetric capacity (678 mA·h/g) and volumetric capacity (3268 mA·h/cm³). In that work, we reported, for the first time, that Se represented an attractive cathode material for not only rechargeable lithium ion batteries but also sodium batteries. Notably, unlike the existing Na/S batteries that only operate at high temperatures,[16,17] these new Se-based electrodes are capable of cycling against Na at room temperature. This encouraging result indicated that the selenium system possesses favorable electrochemical properties compared to its sulfur analogues. However, there are still some fundamental issues that need to be clarified. For example, the

charge and discharge voltages are evolving in the Li/Se system during the initial cycles in the carbonate-based electrolyte. Significant polarization occurs once the charge and discharge voltages are stabilized after five cycles, which leads to a low roundtrip efficiency. In addition, the Coulombic efficiency is quite low during the first 20 cycles. The mechanisms or underlying reasons for this unsatisfactory performance are still not well understood due to inadequate characterization of the battery materials during electrochemical cycling. In particular, the effects of organic electrolytes on the (de)lithiation process (i.e., both lithiation and delithiation) of the Li/SeS_x cells, if any, are still not clear, nor are the effects of the sulfur content in SeS_x.

Organic electrolytes are known to be particularly important in Li/O_2 and Li/S batteries. For instance, the electrolyte plays a key role in Li/O_2 cell performance because, at high voltage, electrolyte decomposition may occur, especially in carbonate-based electrolyte.[10,18] It has also been reported that cycle life could be extended for Li/S batteries by tuning the composition of the electrolyte.[19,20] Selenium, since it is located in the same group as oxygen and sulfur in the periodic table, should exhibit a similar reactivity preference when used as a cathode material. Moreover, the selenium anion is more nucleophilic than the sulfur anion, showing even higher reactivity with carbonyl groups in the traditional carbonate-based electrolyte.[21] We, therefore, expected that performance could be enhanced for the Li/Se system by utilizing a noncarbonate electrolyte, as is the case for Li/S and Li/O_2 batteries.

In this study, we first adopted an ether-based electrolyte in the Li/SeS_x cell to investigate its effect on the electrochemical performance. The results demonstrate that cell performance is significantly improved in terms of voltage profile and Coulombic efficiency. The voltage profiles of these cells indicate that complete lithiation of selenium to Li_2Se is occurring through the formation of intermediate phases, i.e., Li_2Se_n. This behavior differs from the single-phase transition in carbonate-based electrolyte, as reported earlier.[15] This result clearly suggests that cell performance highly depends on the nature of the electrolyte. In order to better understand the relationship between the formation of the intermediate phases and voltage profile of the cells with the ether-based electrolyte, we performed an in-depth study by different characterization techniques, including high-energy X-ray diffraction (HEXRD) and X-ray absorption spectroscopy (XAS). The powerful capability of in situ HEXRD and XAS, available at the Advanced Photon Source (APS) at Argonne National Laboratory, allowed us to monitor instantly the phase transition, the intermediate phases, and their oxidation states during cycling. The mechanism behind the (de)lithiation processes for Li/SeS_x cells is proposed here on the basis of the results obtained from the in situ X-ray probes. This work has helped us to better understand and correlate the formation of intermediate phases with the electrochemical performance of Li/SeS_x cells and shines new light on how to improve the cell performance by tuning the electrolyte composition.

2. EXPERIMENTAL SECTION

2.1. Preparation and Characterization of the Carbon–Selenium Composite. Composite materials were prepared by mixing selenium (or SeS_x) with multiwalled carbon nanotubes (Aldrich) in a 7:3 mass ratio, grinding for 65 h, then heating at 260 °C (or 160 °C for SeS_2- and SeS_7-containing composites) under argon for 16 h. The dry grinding was carried out on a SWECO Vibro-Energy

Grinding Mill with ball to powder ratio of 7:1. The Se and SeS_2 were purchased from Aldrich and used directly. The SeS_7 was synthesized by mixing SeS_2 and S (Aldrich) in a 1:5 ratio and then heating at 160 °C for 16 h. Also, Li_2Se was synthesized by lithium triethylborohydride reduction of selenium pellets in tetrahydrofuran (THF) to serve as a standard material.[22] X-ray diffraction (XRD) patterns indicated that the desired phases were well crystallized, as shown in Figure 1S (Supporting Information).

2.2. Electrochemical Characterization. The electrochemical performance of the selenium−carbon composites was assessed by fabricating CR2032 coin cells. Metallic Li foil was used as the negative electrode. The positive electrode was prepared by first mixing a slurry containing 70 wt % composite material, 10 wt % carbon black, and 20 wt % polyvinylidene fluoride (PVDF) or polytetrafluoroethylene (PTFE) binder, previously dissolved in N-methyl-2-pyrrolidinone (NMP), and the proper amount of NMP as dispersant. The slurry was then coated on aluminum foil using a doctor blade. The NMP was removed by first drying the electrode at 75 °C for 2 h and then further drying the electrode in a vacuum oven at 100 °C overnight. A half-cell was constructed in an argon-filled glovebox. The electrolyte (designated D2) was 1 M lithium bis(trifluoromethanesulphonyl)-imide (LiTFSI) in 1,3-dioxolane (DOL):1,2-dimethoxyethane (DME) (1:1 v/v ratio), and the separator was a Celgard 2325 film. For comparison, several cells were assembled with a carbonate electrolyte (GenII): $LiPF_6$ (1.2 M) dissolved in ethylene carbonate (EC)/ethyl methyl carbonate (EMC) solvents (3:7 v/v ratio). The cells were tested with a MACCOR electrochemical analyzer at a current density of 50 mA/g between 0.8 and 4.0 V. Electrochemical tests were conducted at room temperature and duplicated to check reproducibility. The capacity was calculated on the basis of the active material mass, which corresponds to 49 wt % of the electrode weight.

Cyclic voltammetry (CV) was conducted at a scan rate of 0.2 mV/s in the potential range of 0.8−4.0 V on the cycled cell using a frequency response analyzer (Solartron, model 1400). Electrochemical impedance spectroscopy (EIS) data were collected over a frequency range from 5×10^5 to 2×10^{-2} Hz, with a potential amplitude of 5 mV on the Solartron analyzer.

Pouch cells for in situ XAS measurements were fabricated using the Cell Fabrication Facility at the Argonne National Laboratory with Li metal as the negative electrode.

2.3. X-ray Diffraction. The HEXRD measurements were carried out at Beamline 11-ID-C of the APS. The X-ray wavelength was 0.108 Å. In situ HEXRD patterns were collected with custom-designed coin cells cycled with a MACCOR cycler at a constant rate (about C/6) between 0.8 and 4.0 V. During the charging and discharging, the XRD patterns were collected for 1 min, with 15−26 min intervals, using a Perkin-Elmer 2D X-ray detector. 2D images were converted into a 1D plot of 2θ versus intensity by using the FIT2D program calibrated against a CeO_2 standard.

2.4. X-ray Absorption Spectroscopy. The XAS measurements for the Se K-edge (12 658 eV) were made in transmission mode on the bending-magnet beamline of the APS (20-BM-B and 9-BM-C). The incident beam was monochromatized by using a Si(111) fixed-exit, double-crystal monochromator. In situ XAS experiments were made on the pouch cells cycled with a MACCOR cycler. Standard materials were mixed with boron nitride and then pressed into a self-supported pellet sealed in 50-μm-thick Kapton tape. X-ray absorption near edge structure (XANES) and extended X-ray absorption fine structure (EXAFS) data reduction followed standard methods using the ATHENA software package.[23] The normalized EXAFS data were converted from energy to k-space by k^2 weighting.

2.5. X-ray Photoelectron Spectroscopy (XPS). Selected electrodes were analyzed by XPS using a Kratos Axis Ultra DLD surface analysis instrument. The base pressure of the analysis chamber during these experiments was 3×10^{-10} Torr, with operating pressures around 1×10^{-9} Torr. Spectra were collected with a monochromatic Al Kα source (1486.7 eV) and a 300×700 μm spot size. The Al source was operated at 12 mA of emission current with the target anode set to 15 kV; the resulting power was 180 W. For survey spectra the data were collected at a pass energy of 160 eV (fixed analyzer
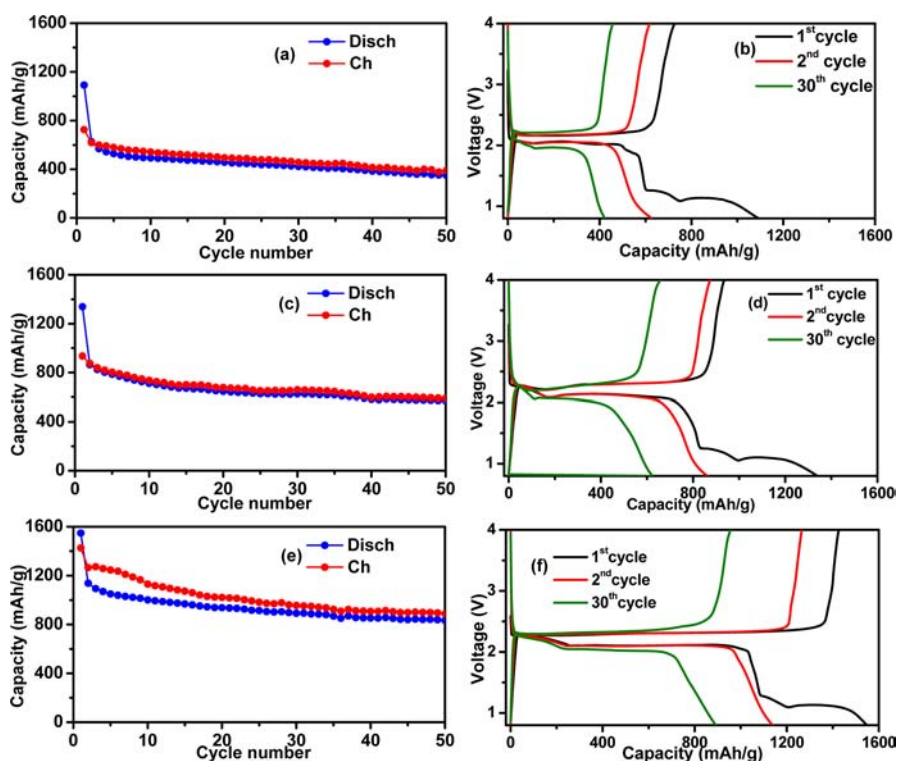
Figure 1. Cycle performance of Li cells with (a, b) Se−, (c, d) SeS$_2$−, and (e, f) SeS$_7$−carbon composite as cathodes in ether-based electrolyte. The second discharge capacities for Li/Se, Li/SeS$_2$, and Li/SeS$_7$ cells are ∼0.6, ∼0.6 and ∼0.9 mA·h/cm^2, respectively.

transmission mode), a step size of 1 eV, and a dwell time of 200 ms. High-resolution regional spectra were collected with pass energy of 20 eV (fixed analyzer transmission mode), a step size of 0.1 eV, and a dwell time of 300 ms. For low signal-to-noise regions, multiple passes were made, and the results averaged. Peak position correction was further corrected by referencing the C 1s peak position of adventitious carbon for a sample (284.8 eV[24]) and shifting all other peaks in the spectrum accordingly.

Fitting was done by using the program CasaXPS. Each relevant spectrum was fit to a Shirley-type background to correct the rising edge of the backscattered electrons, which shift the baseline higher at high binding energies. Peaks were fit as asymmetric Gaussian/Lorentzian line shapes, with 0−30% Lorentzian character. The full width at half-maximum of all subpeaks was constrained to 0.7−2.0 eV, as dictated by instrumental parameters, lifetime broadening factors, and broadening due to sample charging. With this native resolution set, peaks were added, and the best fit was obtained from a least-squares fitting routine.

3. RESULTS AND DISCUSSION

3.1. Electrochemical Performance in Ether-Based Electrolyte. Active cathode materials containing Se, SeS$_2$, and SeS$_7$ combined with carbon were tested against Li metal anodes between 0.8 and 4.0 V, and the capacity retention over 50 cycles is shown in parts a, c, and e of Figure 1, respectively. The ether-based electrolyte D2, i.e., 1.0 M LiTFSI in DOL/DME, was selected for this study due to its greater stability compared to the carbonate-based electrolyte in Li/O$_2$ and Li/S systems. A discharge capacity of 350, 571, and 833 mA·h/g for the Li/Se, Li/SeS$_2$, and Li/SeS$_7$ cells, respectively, is maintained for over 50 cycles. The cell capacity increases with increasing S content in the composites due to its contribution to the overall capacity. The capacity faded a little for all three cells tested. The Coulombic efficiency was nearly 100% for the Li/Se and Li/SeS$_2$ cells. The Li/SeS$_7$ cell showed a relatively low Coulombic

efficiency during the initial 20 cycles, although much higher capacity. This behavior is likely due to the greater amount of S in the SeS$_7$ compound. The Li/(Se + 2S) and Li/S cell were also tested, as shown in Figures 2S and 3S (Supporting Information), for comparison. Among the three composite materials tested in this study, SeS$_2$ showed the most favorable trade-off among capacity, efficiency, and capacity retention.

Parts b, d, and f of Figure 1 present the first, second, and 30th voltage profiles of these same three cells. These profiles suggest overall reversible electrochemical reactions for all the cells. In the case of the Li/Se cell (Figure 1b), two voltage plateaus are visible above 1.5 V in the discharge profiles with an inflection point at about 2.03 V vs Li$^+$/Li. This finding implies that multistep phase transitions take place during the discharge when the ether-based electrolyte is applied, since a single-step reaction was detected for the same composite using the carbonate-based electrolyte, as we reported earlier.[15] This observation indicates that the intermediate phases and their solubility are varied in different electrolytes. Upon charging, a single plateau at about 2.2 V is present for the Li/Se cell. Comparable discharge and charge plateau potentials are also present for the Li/SeS$_2$ and Li/SeS$_7$ cells. The voltage profiles shown in Figure 1b,d,f indicate that the polarization of the cells is significantly reduced in comparison to that for the carbonate-based electrolyte, which leads to the higher efficiency of the cells in the ether-based electrolyte. Note that the voltage variation below 1.5 V in the first discharge profile is ascribed to the decomposition of the PTFE binder, since it is not observed with the use of PVDF binder. This conclusion is confirmed by the XPS analysis on the Se cathode after the first discharge, as shown in Figure 4S (Supporting Information). A clear Li−F signal in the F 1s XPS spectrum is present due to the decomposition of the PTFE binder, which is less stable than PVDF in the low-voltage range when used as a binder for the
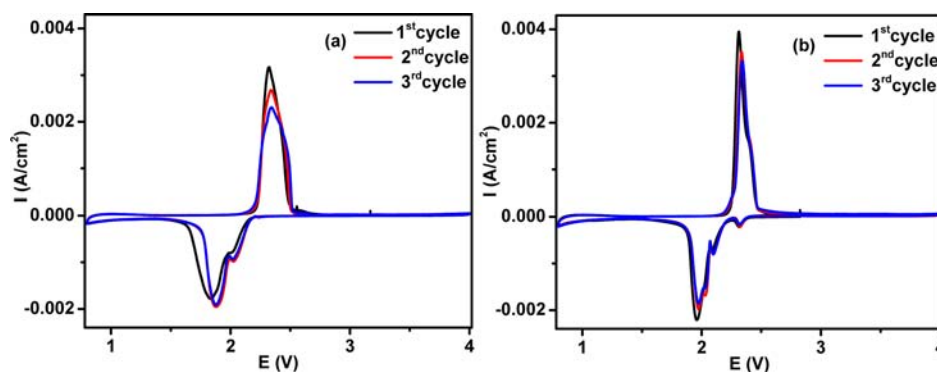
Figure 2. Cyclic voltammetry curves of (a) Li/Se and (b) Li/SeS$_2$ batteries in ether-based electrolyte with PVDF binder.
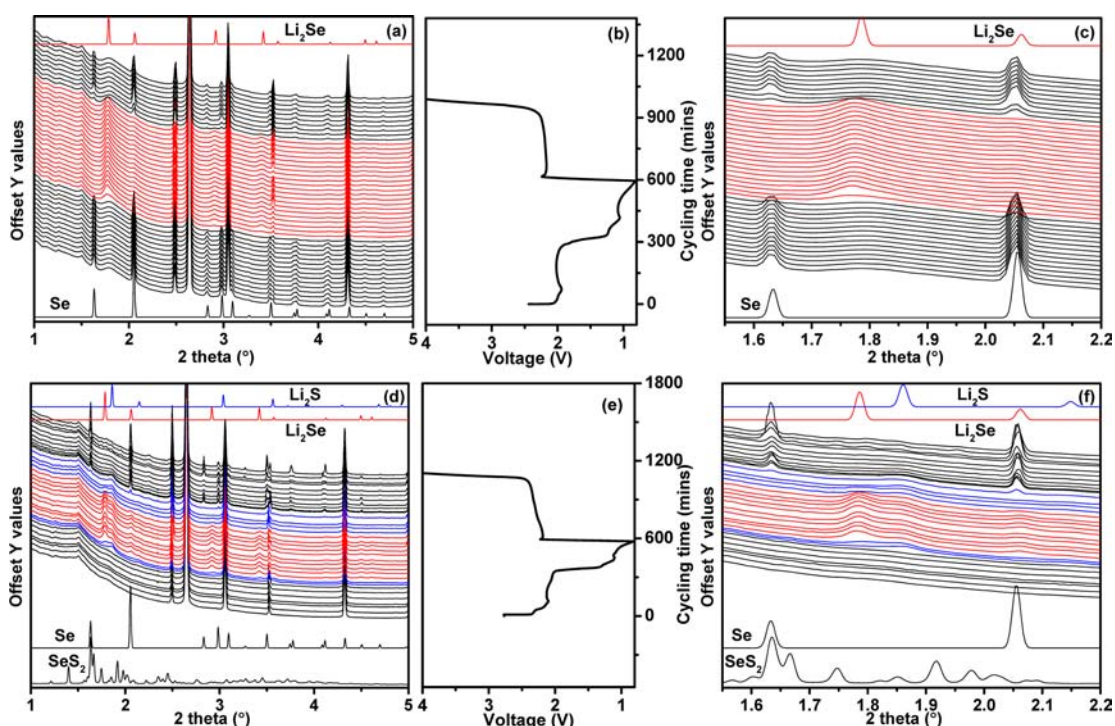

Figure 3. HEXRD patterns of Li/Se cell during the first cycle (a, c) with the voltage profile (b). HEXRD patterns of Li/SeS$_2$ cell in the first cycle (d, f) with the voltage profile (e).

anode applications.[25] We only observed the decomposition of PTFE in the first discharge, and the cell reaction stabilized afterward. Because the PTFE-containing cathode had showed better capacity retention and cycle life than those with PVDF binder,[26] we adopted this binder for cycle testing of the cells. To avoid the complexity introduced by the PTFE binder during the further characterizations of the cells, including CV and in situ XAS, as presented below, PVDF binder was applied instead.

The CV curves for the Li/Se and Li/Se$_2$S cells are shown in Figure 2. In the Li/Se system, the CV starts from an open circuit voltage of 3.2 V and sweeps to 0.8 V during the initial discharge, converting elemental selenium to selenides with two reduction peaks at 1.83 and 2.02 V. These features are analogous to those of Li/S cells, in which two separate reduction peaks at 2.4 and 2.1 V were observed, corresponding to the conversion of high-order lithium polysulfides (e.g., Li$_2$S$_8$) to low-order lithium polysulfides (Li$_2$S$_x$, 8 > x ≥ 4) and then to Li$_2$S$_2$/Li$_2$S, respectively. In the subsequent anodic sweep to 4.0 V, only one oxidation peak at 2.32 V is observed for the Li/Se

system. In the Li/S system, some studies suggest that since only one oxidation peak is observed at 2.5 V, the "recovered" product after the charge should be intermediate S$_8^{2-}$ instead of elemental S.[27−29] On the basis of the CV results and the similarity between Se and S, we can propose a mechanism for the electrochemical reactions in the Li/Se cell that has been further confirmed by the in situ X-ray probes, as will be presented in the later sections of this paper.

According to this mechanism, during the discharge, elemental Se is first reduced to lithium polyselenide Li$_2$Se$_n$ (n ≥ 4), which is further reduced to Li$_2$Se$_2$ and Li$_2$Se, while the discharge product Li$_2$Se is oxidized into intermediate polyselenides Li$_2$Se$_n$ (n ≥ 4) and Se during the subsequent charge. In addition, the two reduction peaks of the following two cycles are relatively stable, while the oxidation activity decreases significantly, indicating improved Coulombic efficiency with cycling. As for the Li/SeS$_2$ cell, the CV curve shows four reduction peaks: peaks at 2.32 and 2.03 V can be assigned to the conversion of high-order polysulfides (due to the introduction of sulfur) to low-order polysulfides and then to
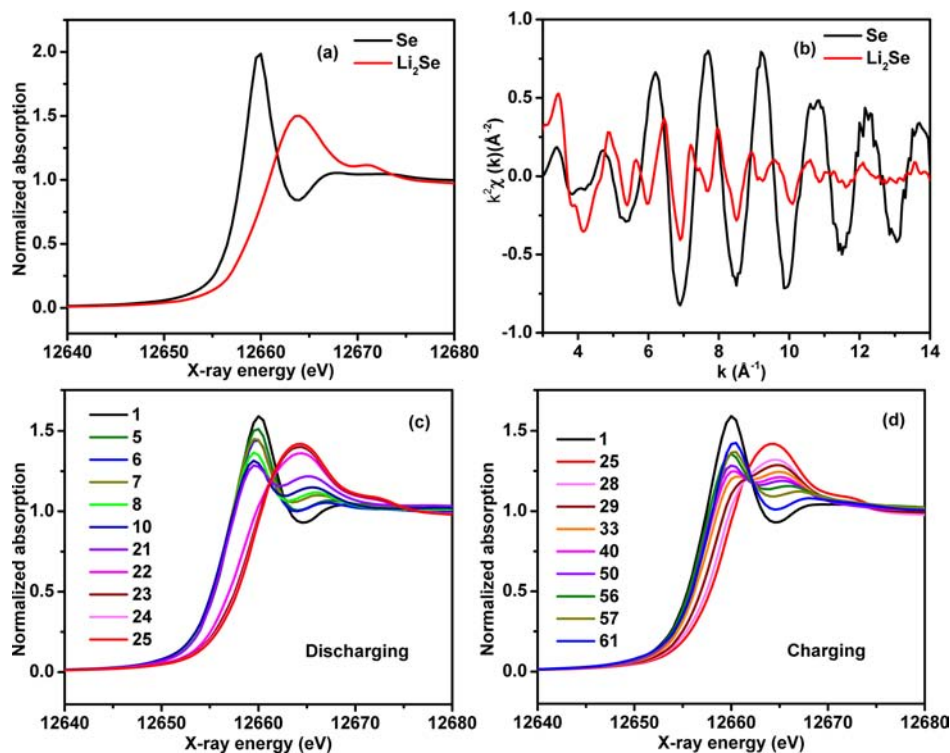
Figure 4. (a) Normalized Se XANES spectra of standard Se and Li$_2$Se, (b) Se EXAFS spectra of standard Se and Li$_2$Se, and also selected normalized Se XANES spectra of Li/Se cell during discharge (c) and charge (d).

Li$_2$S$_2$ and Li$_2$S, and peaks at 2.10 and 1.95 V can be attributed to the conversion of Se to polyselenides and then to Li$_2$Se. Correspondingly, two oxidation peaks at 2.30 and 2.39 V during the charge sweep are attributed to the oxidation of Li$_2$Se and Li$_2$S, respectively. To better understand the lithium (de)insertion mechanism of the Se-containing material in the ether-based electrolyte, in situ HEXRD and XAS investigations were carried out on Se and SeS$_2$ composites.

3.2. In Situ HEXRD Analysis. In situ HEXRD is a powerful technique for monitoring reacting systems, since it can produce high-quality data in a very short time period (e.g., 1 min or even less depending on the material properties). Specially designed coin cells were used for the in situ HEXRD studies. High-energy X-rays, which can penetrate the Al current collector and the Li foil anode, make the measurements possible. The resulting HEXRD patterns revealed a few very strong peaks at 2.65°, 3.05°, and 4.32° for the Al current collector and 2.50°, 3.53°, and 4.32° for the Li anode. Figure 3 shows the HEXRD patterns for the Se and SeS$_2$ composites in lithium coin cells during cell cycling. As shown in Figure 3a,b, the peak intensity of the starting material, Se, decreased, while the Li$_2$Se peaks were growing during the discharging, and the process was reversed during charging, even though the peak intensities for Se and Li$_2$Se are relatively low compared to the peaks for the Al current collector.

An enlarged portion of the HEXRD patterns (Figure 3c) exhibits additional details about the phase change. The intensity of the Se peaks (1.64° and 2.06°) decreases slowly with the lithiation process, while no new phase appears until the cell is discharged to ~1.69 V. The voltage quickly drops to ~1.25 V after a 26-min measurement interval. The Li$_2$Se phase starts to appear when the Se peaks have completely vanished. During the charge, the Li$_2$Se phase remains until the potential reaches ~2.22 V. When charging to 2.24 V, the Se structure starts to

grow steadily with accompanying disappearance of Li$_2$Se. During the discharge, the amount of crystalline Se decreases with Li insertion; however, Li$_2$Se does not form until a capacity of ~500 mA·h/g is reached without any other phases detected. At this point, several questions arose concerning where the Li$^+$ goes during discharging, why Li$_2$Se forms only after a critical potential of 1.25 V, and/or whether Li$_2$Se forms earlier as an amorphous phase. We could not resolve these questions conclusively on the basis of the HEXRD analysis, since it can only detect crystalline phases.

For SeS$_2$, as shown in Figure 3d−f, no crystalline phase is present at the beginning of discharge. When the cell is discharged to 2.08 V, the Li$_2$S phase first appears followed by Li$_2$Se crystallization at ~2.04 V. During the delithiation, Li$_2$Se and Li$_2$S remain until the cell is charged to 2.19 and 2.30 V, respectively. When the cell is charged to 2.25 V, Se peaks appear and keep increasing to the end of charge. These phenomena suggest that the charge product is a mixture of Se and S, but the S is not detected due to its weak diffraction ability. Other evidence for the charge products come from the high capacity of the Li/SeS$_2$ cell obtained in the second cycle and the HEXRD of the second discharge, which show the presence of Li$_2$Se and Li$_2$S (Figure 5S, Supporting Information).

3.3. In Situ XANES Analysis. Synchrotron radiation based XAS is a well-established method to probe the environment around atoms of all states of matter.[30] In situ XAS can be very informative when applied to a complex battery system that involves liquid and solid, as well as crystalline and/or amorphous phases. Also XANES is especially useful for determining the average oxidation state of the elements in all phases. With these considerations in mind, we carried out XAS measurements during cycling of a pouch cell. As shown in Figure 4a, the two curves are XANES from commercial
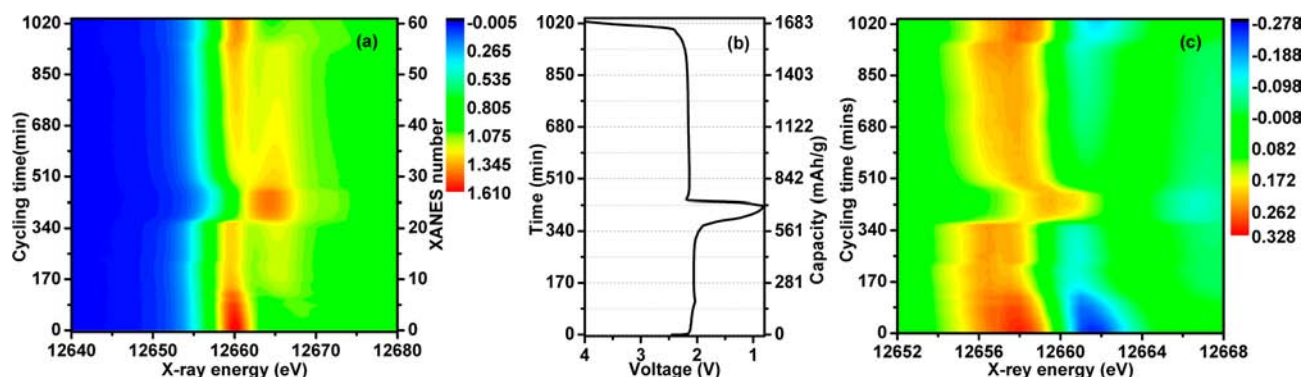
Figure 5. (a) Normalized XANES spectra of Li/Se cell during cycling, (b) battery voltage profile, and (c) derivative of normalized XANES spectra of Li/Se cell during cycling.
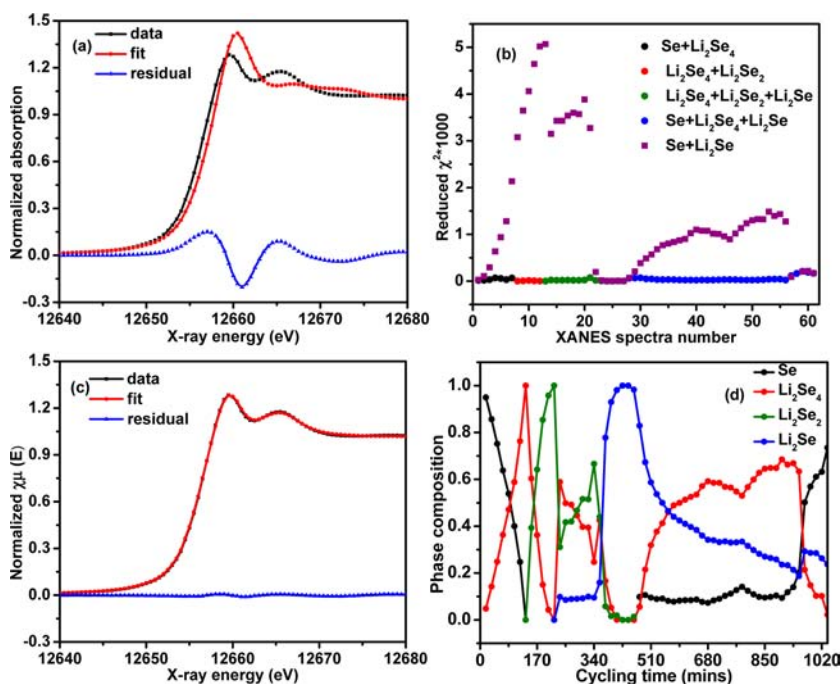

Figure 6. Se XANES spectra linear combination fitting, (a) XANES 19th spectrum fitted with two components (Se and Li_2Se) showing huge residue, (b) reduced $\chi^2 \times 1000$ of the linear combination fitting of XANES spectra using different component combinations, (c) XANES 19th spectrum fitted with three components (Li_2Se_4, Li_2Se_2, and Li_2Se), and (d) relative composition evolution of possible phases during cycling.

selenium powder and synthesized Li_2Se mixed with boron nitride. The selenium K-edge absorption, at 12 658 eV, arises from the transition of Se 1s core electrons to the unoccupied 4p states.[31] The Se K-edge of Li_2Se shifts to a higher energy at 12 660 eV, which is inconsistent with the commonly observed phenomenon that the edge shifts to a higher energy with the increasing oxidation state.[31,32] However, that the Se K-edge of Li_2Se shifts to a high energy might also be explained by a reduced screening effect, as in the S case.[20] The S K-edge of Li_2S shifted to a higher energy, as reported by Abruna et al. in 2011, due to the strong Coulombic interaction between the S^{2-} ion and the eight neighboring Li^+ ions, which reduces the screening effect.[20,33] In addition, the change in composition from Se to Li_2Se can be seen in k-space as the shape of the EXAFS spectra changes significantly (Figure 4b). Figure 4c,d compare selected XANES spectra from the first discharge and charge of the Li/Se cell. To better illustrate the XANES spectra evolution, 2D contour plots of Se XANES spectra recorded during the cell cycling are presented in Figure 5a. In addition,

the Li/Se battery voltage profile is displayed on the side of the XANES spectra (Figure 5b). During lithiation, the critical points (at 2.04 and 1.67 V) of the electrochemical process are well-correlated with the evolution of the XANES spectra. For example, the inflection point at 2.04 V in the voltage profile coincides with the shift of the XANES spectrum to lower energy. The precipitous voltage drop at around 6 h of discharging corresponds to the sudden appearance of the Se K-edge of Li_2Se.

Generally, the energy position of the edge is determined as the lowest energy peak of the first derivative of the XANES spectra. To determine the edge positions, we show the first derivatives of the XANES spectra in Figure 5c. This plot shows that the Se edges are shifted significantly with (de)lithiation. When the cell is first discharged through the inflection point at 2.04 V, the edge shifts from 12 657.9 to 12 656.7 eV. In the following 3 h (more than 300 mA·h/g capacity), the edge positions do not change much and are accompanied by the voltage plateau around 2 V. When the cell is discharged to 1.67
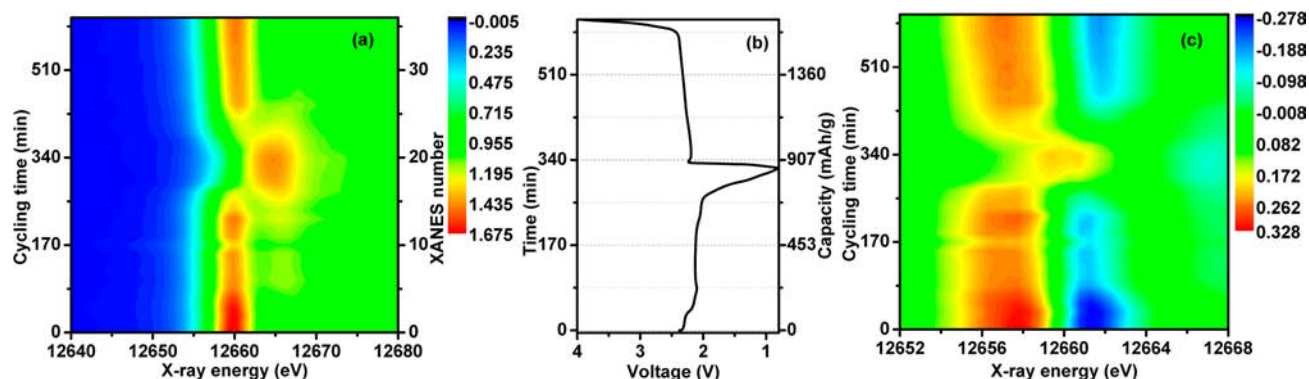
Figure 7. (a) Normalized XANES spectra, (b) voltage profile, and (c) derivative of normalized XANES spectra of Li/SeS_2 cell during cycling.
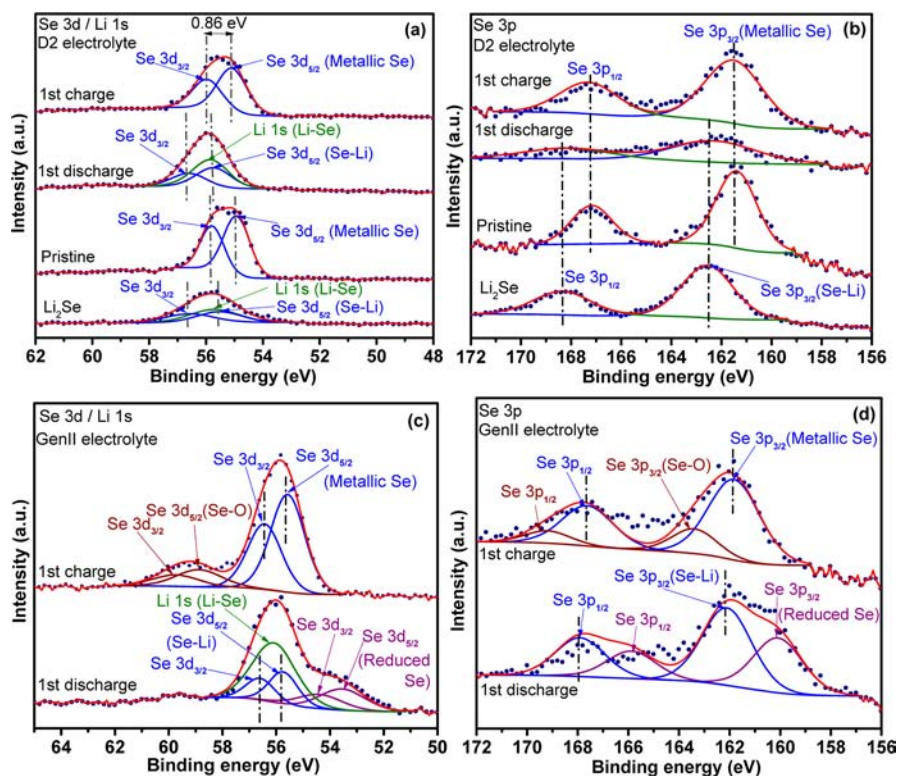

Figure 8. XPS spectra of Se cathodes with different electrolytes: (a) Se 3d/Li 1s and (b) Se 3p for 1 M LiTFSI in DOL/DME (D2) as electrolyte, and (c) Se 3d/Li 1s and (d) Se 3p for 1.2 M $LiPF_6$ in EC/EMC (GenII) as electrolyte.

V, the Se K-edge jumps to 12 660 eV, suggesting the formation of Li_2Se. During charge, the Se edges slowly shift back to lower energy. These observations indicate that polyselenides might have formed during the cycling, but in a noncrystalline state; hence, they are not detected by XRD. At the beginning of the discharge, Se reacts with Li^+ ions, forming polyselenides and leading to the decrease of Se concentration seen in the in situ HEXRD studies. As a consequence, the reduced Se in the lithium polyselenides shifts the Se K-edge to a lower energy, as expected. With increasing lithiation, the elemental Se is depleted, and polyselenides are reduced to crystallized Li_2Se, which contains Se^{2-} ions in an environment surrounded by eight Li^+. The strong Coulombic interaction significantly reduces the screening effect and shifts the Se edge to a higher energy.

Another common use of XANES is for fingerprinting by linear combination fitting of XANES spectra of known species to determine the components in a mixture.[34] Linear combination fitting is conveniently available in the Athena software package.[23] By selecting XANES spectra of the starting materials and discharge products as standards, we can determine the composition of the electrodes at different states of charge by linear combination fitting. With the hypothesis that we have a two-phase, one-step transition from Se to Li_2Se directly, we first fit all the spectra using the spectrum of the pristine electrode and the 25th spectrum measured at the fully discharged point as standards. Unfortunately, most of the spectra could not be well fitted; Figure 6a is an example of a poorly fitted spectrum, as illustrated by the large reduced χ^2 from 0.020‰ to 5.676‰ shown in Figure 6b (purple squares). However, when carrying out the fitting on any combination of Se, Li_2Se, Li_2Se_n ($n \geq 4$), and Li_2Se_2 as standards, we achieved greatly improved fits, with reduced χ^2 values from 0.017‰ to 0.07‰, as also shown in Figure 6b. Details of the standards selection procedure are discussed in the Supporting Information. An example of a good fit is plotted in Figure 6c. The

relative composition of each component in the process of cycling is shown in Figure 6d. The exact value of the composition may not be completely accurate, considering the standards selection procedure. However, the trend for each component's evolution is of significance. For example, with Se composition decreasing, Li_2Se_n ($n \geq 4$) forms, increases in content, and then decreases with Li_2Se_2 formation (Figure 6d). During discharge, Li_2Se_n ($n \geq 4$), Li_2Se_2, and Li_2Se coexist. The fully charged electrode has a composition of 74% Se, 2% Li_2Se_n ($n \geq 4$), and 24% Li_2Se, as indicated by the fully charged Se edge being about 0.2 eV higher than the pristine Se edge. This finding suggests that some Li_2Se might have formed on the anode side due to the dissolution of polyselenides. This hypothesis is supported by Raman spectra, as Li_2Se was observed on the Li anode of the charged cells (Figure 6S, Supporting Information).

In situ Se XANES measurement on a Li/SeS_2 cell was also carried out at APS Sector 9. A 2D contour plot of Se XANES spectra of the cycled cell is shown in Figure 7a, with the corresponding voltage profile plotted in Figure 7b. These results further confirm that SeS_2 is reduced to Li_2Se and Li_2S with the Se K-edge shifting to higher energy. The 2D contour plot of the first derivative of the XANES spectra also exhibits a slight shift of the Se K-edge to lower energy, with the formation of lithium polyselenides, followed by a jump to higher energy, indicating the formation of Li_2Se (Figure 7c), as observed in the Li/Se case.

3.4. XPS and EIS Analysis. We also performed XPS analysis, a surface sensitive technique that can provide valuable information about the solid reaction products on the cathode surface. We derived high-resolution C 1s, F 1s, Li 1s, Se 3d, and Se 3p XPS spectra of the cathodes from the Li/Se system with the two electrolytes. The C 1s peak position of adventitious carbon at 284.8 eV was used as an internal reference. The fitted Li 1s, Se 3d, and Se 3p XPS spectra are shown in Figure 8. Note that, because the XPS spectra of Li 1s and Se 3d overlap, we provided XPS spectra of Se 3p as additional evidence for Se evolution between discharge and charge.

Figure 8a,b shows the Se 3d (Li 1s) and Se 3p XPS spectra for cathodes recovered from the first discharge and first charge using the ether-based (D2) electrolyte. For comparison, the XPS spectra of the pristine Se cathode and Li_2Se powder are also shown at the bottom of these figures. In the pristine Se cathode, Se $3d^{5/2}$ and $3d^{3/2}$ peaks (Figure 8a) located at ~55.2 and ~56.1 eV with a spin−orbit splitting of 0.86 eV are attributed to metallic selenium.[24] The Se $3d^{5/2}$ peak moves toward higher binding energy (about 55.6 eV) when Se binds with Li, forming Li_2Se. This trend is consistent with the Se 3p (Figure 8b) XPS spectra, as well as with the XANES results presented earlier. On the basis of both Se 3d/Li 1s and Se 3p XPS spectra, as shown in Figure 8a,b, Li_2Se appears to form as the dominant discharge product of the electrochemical reactions. After the first charge, the Li 1s signals from Li_2Se completely disappear (Figure 8a), and the Se 3p peak moves back to the binding energy for metallic Se (Figure 8a), suggesting that Li_2Se reversibly oxidizes to Se. This encouraging result suggests that the desired discharge products (Li_2Se) can be produced without any side reactions on the electrode surface when the D2 electrolyte is used. It is noteworthy that this is not the case with carbonate-based electrolyte.

After the first discharge and the first charge, the Se 3d (Li 1s) and Se 3p XPS spectra of cathodes using the GenII electrolyte showed extra peaks, as evident in Figure 8c,d. The reversible

reaction between Se and Li_2Se is also observed during the first cycle, but at the end of the discharge, the presence of a peak at lower binding energy can be related to a reduced selenium species other than Li_2Se. After the first charge, the peaks at higher binding energy could be attributed to Se−O species. The Se−O species might form as a result of the reaction of Se anions with the carbonyl groups of the carbonate solvent. Such reactions, because of the formation of an insulating layer on the cathode surface that impedes the transportation of lithium ions and electrons, will lead to poor cycle performance and large overpotential, as reported earlier.[15]

Electrochemical impedance spectroscopy (EIS) provides further evidence for the formation of an insulating layer on the electrode surface of Li/Se cell with GenII electrolyte. The EIS data were obtained right after the cell assembly and after five cycles with D2 and GenII electrolyte (selected voltage profiles with different electrolyte are compared in Figure 7S, Supporting Information). The Nyquist plots for the Li/Se cells (Figure 9) are composed of a semicircle at high frequencies and
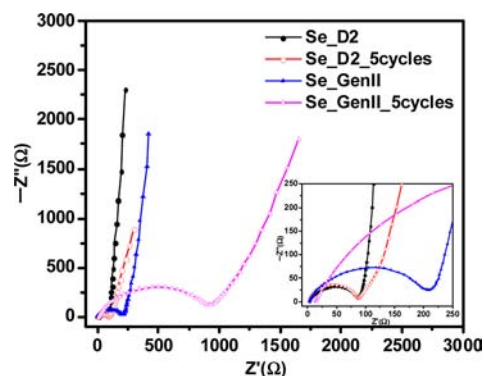

Figure 9. Nyquist plots after fabrication of Li/Se cell and after five cycles with LiTFSI in DOL/DME (D2) or $LiPF_6$ in EC/EMC (GenII) as electrolyte.

an inclined line at low frequency. The intercepts of the semicircles and the real axis can be used to determine the resistance of the electrolyte (R_e, in the high-frequency region) and the resistance to charge transfer (R_{ct}, at relatively lower frequency). The data show that the resistances (both R_e and R_{ct}) of the Li/Se cell with D2 electrolyte barely changed after five cycles. For the cell with GenII electrolyte, the R_e of the fresh cell is comparable to that of the cell with D2 electrolyte, but it increased after five cycles, indicating the instability of the carbonate-based electrolyte. The R_{ct} of the fresh cell in the G2 electrolyte is more than twice that of the cell with D2 electrolyte and increases to more than 10 times larger with the D2 electrolyte after five cycles. These findings can be ascribed to an insulting layer formed on the cathode, as observed in the XPS analysis. These results further illustrate the advantage of D2 electrolyte over GenII electrolyte.

4. (DE)LITHIATION MECHANISM

We can now propose a mechanism for the Li/Se cell lithiation process by correlating the voltage profiles, the linear combination fitting of the XANES spectra, and the HEXRD analysis. Figure 10 shows the proposed mechanism in the form of a voltage profile with the associated phases that form during charge and discharge. Selenium is first reduced to Li_2Se_n ($n \geq 4$) at 2.04 V, which is then further reduced to Li_2Se_2 and Li_2Se after discharging to 2.06 and 0.8 V, respectively. During
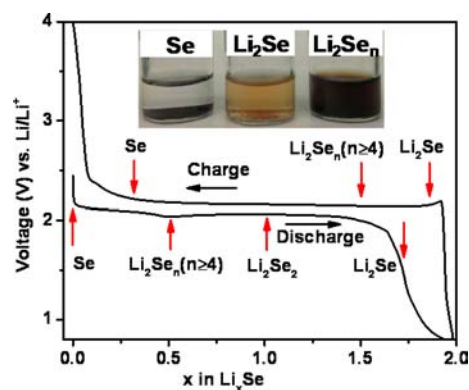
Figure 10. Representation of cathode phase evolution during charge and discharge of a Li/Se cell in an ether-based electrolyte.

charging, Li_2Se is directly oxidized to Li_2Se_n ($n \geq 4$) and then Se. We believe that the only oxidation peak in the CV curve (Figure 2a) actually corresponds to two processes: Li_2Se to Li_2Se_n ($n \geq 4$) and Li_2Se_n ($n \geq 4$) to Se. Due to the different kinetics of the processes, the two oxidation peaks completely overlap. This mechanism is quite similar to that of the Li/S battery, which shows two reduction peaks, ascribed to the reduction of high-order polysulfide (e.g., Li_2S_8) to low-order polysulfides (Li_2S_x, $8 > x \geq 4$) and polysufides to Li_2S_2 and Li_2S, where the one oxidation peak is attributed to the oxidation of Li_2S to polysulfides without the formation of S.[27−29] In our HEXRD and XANES results, we did see the Se recovery after charge, as well as the coexistence of Li_2Se_n ($n \geq 4$), Li_2Se, and Se. This difference between S and Se is related to the high atomic number of Se, which is easily detected by various techniques, such as XRD and XANES, in contrast to S.

To further demonstrate the formation of lithium polyselenides, we completed a solubility test. We added 3.95 mg of Se to 5 mL of DOL and DME solvent (equivalent to 0.01 mol/L solution) in one container and 4.64 mg of Li_2Se to 5 mL of the same solvent in a second container (again equivalent to 0.01 mol/L solution). As shown in the inset of Figure 10, neither material is completely dissolved when present alone, the solubility of Se being extremely low. However, the precipitated Se particles did dissolve when we added a few drops of saturated Li_2Se solution to the Se suspension, and the solution took on a dark brown color. The intense color of the solution suggests the formation of highly soluble polyselenides.[35] Polyselenide speciation studies had been carried out as early as 1977 with various techniques, such as ultraviolet−visible spectroscopy, nuclear magnetic resonance, electrospray mass spectrometry, and electrochemical techniques.[35−40] Accordingly, Se_n^{2-} species with $n = 1-8$ were identified.[35,37,38,40] This test confirmed that the lithium polyselenides do exist in D2 electrolyte and are more soluble than either Se or Li_2Se alone. We believe that the formation of soluble polyselenides could facilitate the Li/Se battery redox reaction, but it may also cause some dissolutive transport of Se to the anode, which would result in the loss of active cathode material, as observed in the Li/S system.[14,41]

5. CONCLUSIONS

A combination of HEXRD and XANES analysis has been used to investigate the (de)lithiation mechanism of the Li/SeS_x cell system. The total conversion of Se into Li_2Se with discharge and recovery of Se with charge was monitored by in situ HEXRD. Complementary XANES spectra analysis provides detailed evidence on the evolution of the selenium valence state in both crystalline and noncrystalline phases during cycling. It is proved that Se is first reduced into polyselenides, Li_2Se_n ($n \geq 4$), then Li_2Se_2, and finally Li_2Se with discharge. During the charge, Li_2Se is directly oxidized to Li_2Se_n ($n \geq 4$) and Se without the formation of Li_2Se_2. The existence of the polyselenides is further manifested by a solubility test of oversaturated Se and Li_2Se solutions in the electrolyte solvent and a mixture of the solutions. The solubility of polyselenides could facilitate the electrochemical reaction in the Li/Se cell but may cause the deposition of Li_2Se on the lithium anode. In addition, we demonstrated that the performance of the Li/SeS_x system is greatly improved by using the ether-based electrolyte. In D2 electrolyte, the Li/SeS_x cell shows reversible cycle performance with a longer cycle life and improved efficiency compared to those assembled with carbonate-based electrolyte. For Li/SeS_2 and Li/SeS_7 cells, Li_2Se and Li_2S are the discharged products, with the presence of Se only as the crystalline phase in the end of charge. More than 350, 571, and 833 mA·h/g discharge capacities were retained after 50 cycles for Li/Se, Li/SeS_2, and Li/SeS_7 cells, respectively. Carbonate-based electrolyte is unstable for Li/SeS_x systems, as shown by XPS and confirmed further by EIS measurements, which showed significant increase of the cell impedance. This phenomenon is quite comparable to the Li/O_2 and Li/S battery systems, where the instability of the carbonate-based electrolyte has been reported.

In this study, we carried out a comprehensive investigation of selenium-based lithium battery systems. In situ XANES provides valuable information on the oxidation states of crystalline and amorphous phases, including intermediate species dissolved in the electrolyte. A mechanism is proposed by a combination of in situ synchrotron X-ray techniques and electrochemical methods. These results also highlight the importance of appropriately combining advance measurement techniques and the wide range of issues in other lithium ion battery systems or other complicated processes that could be investigated by these combined techniques.

■ ASSOCIATED CONTENT

Ⓢ Supporting Information

XRD patterns for synthesized SeS_7 and Li_2Se, cycle performance of Li/S and (Se + 2S)−carbon composite materials, F 1s XPS spectra of pristine Se cathode with PTFE binder and after first discharge, in situ HEXRD patterns of Li/SeS_2 cell in the second cycle, XANES spectra linear combination fitting polyselenide standards selection procedures, Raman spectra of Li_2Se powder and a charged anode recovered from a Li/Se cell with D2 electrolyte, and voltage profile comparison of Li/Se cell with LiTFSI in DOL/DME (D2) or $LiPF_6$ in EC/EMC (GenII) as electrolyte. This material is available free of charge via the Internet at http://pubs.acs.org.

■ AUTHOR INFORMATION

Corresponding Author

abouimrane@anl.gov

Notes

The authors declare no competing financial interest.

■ REFERENCES

(1) Tarascon, J. M.; Armand, M. *Nature* **2001**, *414*, 359.
(2) Whittingham, M. S. *Chem. Rev.* **2004**, *104*, 4271.
(3) Rao, M. L. B. U.S. Patent 3413154, 1968.
(4) Ji, X.; Lee, K. T.; Nazar, L. F. *Nat. Mater.* **2009**, *8*, 500.
(5) Zhang, B.; Qin, X.; Li, G. R.; Gao, X. P. *Energy Environ. Sci.* **2010**, *3*, 1531.
(6) Abraham, K. M.; Jiang, Z. *J. Electrochem. Soc.* **1996**, *143*, 1.
(7) Ogasawara, T.; Debart, A.; Holzapfel, M.; Novak, P.; Bruce, P. G. *J. Am. Chem. Soc.* **2006**, *128*, 1390.
(8) Read, J. *J. Electrochem. Soc.* **2002**, *149*, A1190.
(9) Peng, Z. Q.; Freunberger, S. A.; Chen, Y. H.; Bruce, P. G. *Science* **2012**, *337*, 563.
(10) Freunberger, S. A.; Chen, Y.; Peng, Z.; Griffin, J. M.; Hardwick, L. J.; Bardé, F.; Novák, P.; Bruce, P. G. *J. Am. Chem. Soc.* **2011**, *133*, 8040.
(11) Padbury, R.; Zhang, X. *J. Power Sources* **2011**, *196*, 4436.
(12) Yeon, J.-T.; Jang, J.-Y.; Han, J.-G.; Cho, J.; Lee, K. T.; Choi, N.-S. *J. Electrochem. Soc.* **2012**, *159*, A1308.
(13) Mikhaylik, Y. V.; Akridge, J. R. *J. Electrochem. Soc.* **2004**, *151*, A1969.
(14) Yamin, H.; Gorenshtein, A.; Penciner, J.; Sternberg, Y.; Peled, E. *J. Electrochem. Soc.* **1988**, *135*, 1045.
(15) Abouimrane, A.; Dambournet, D.; Chapman, K. W.; Chupas, P. J.; Weng, W.; Amine, K. *J. Am. Chem. Soc.* **2012**, *134*, 4505.
(16) Rydh, C. J.; Sanden, B. A. *Energy Convers. Manage.* **2005**, *46*, 1957.
(17) Lu, X.; Kirby, B. W.; Xu, W.; Li, G.; Kim, J. Y.; Lemmon, J. P.; Sprenkle, V. L.; Yang, Z. *Energy Environ. Sci.* **2013**, *6*, 299.
(18) Mizuno, F.; Nakanishi, S.; Kotani, Y.; Yokoishi, S.; Iba, H. *Electrochemistry* **2010**, *78*, 403.
(19) Chang, D.-R.; Lee, S.-H.; Kim, S.-W.; Kim, H.-T. *J. Power Sources* **2002**, *112*, 452.
(20) Gao, J.; Lowe, M. A.; Kiya, Y.; Abruna, H. D. *J. Phys. Chem. C* **2011**, *115*, 25132.
(21) Steinmann, D.; Nauser, T.; Koppenol, W. H. *J. Org. Chem.* **2010**, *75*, 6696.
(22) Detty, M. R.; Seidler, M. D. *J. Org. Chem.* **1982**, *47*, 1354.
(23) Ravel, B.; Newville, M. *J. Synchrotron Radiat.* **2005**, *12*, 537.
(24) Moulder, J. F.; Stickle, N. F.; Sobol, P. E.; Bomben, K. D. (Eds.) *Handbook of X-ray Photoelectron Spectroscopy*; Physical Electronics Inc. (PHI): Eden Prairie, MN, 1995.
(25) Liu, W.; Huang, X.; Li, G.; Wang, Z.; Huang, H.; Lu, Z.; Xue, R.; Chen, L. *J. Power Sources* **1997**, *68*, 344.
(26) Manickam, M.; Takata, M. *Electrochim. Acta* **2003**, *48*, 957.
(27) Ji, X.; Nazar, L. F. *J. Mater. Chem.* **2010**, *20*, 9821.
(28) Fu, Y.; Manthiram, A. *RSC Adv.* **2012**, *2*, 5927.
(29) Yamin, H.; Penciner, J.; Gorenshtain, A.; Elam, M.; Peled, E. *J. Power Sources* **1985**, *14*, 129.
(30) Koningsberger, D. C.; Prins, R. *X-ray Absorption: Principles, Applications, Techniques of EXAFS, SEXAFS and XANES*; John Wiley and Sons: New York, 1988.
(31) Myneni, S. C. B.; Tokunaga, T. K.; Brown, G. E. *Science* **1997**, *278*, 1106.
(32) Pickering, I. J.; Brown, G. E.; Tokunaga, T. K. *Environ. Sci. Technol.* **1995**, *29*, 2456.
(33) Mori, R. A.; Paris, E.; Giuli, G.; Eeckhout, S. G.; Kavcic, M.; Zitnik, M.; Bucar, K.; Pettersson, L. G. M.; Glatzel, P. *Anal. Chem.* **2009**, *81*, 6516.
(34) Lengke, M. F.; Ravel, B.; Fleet, M. E.; Wanger, G.; Gordon, R. A.; Southam, G. *Environ. Sci. Technol.* **2006**, *40*, 6304.
(35) Ahrika, A.; Paris, J. *New J. Chem.* **1999**, *23*, 1177.
(36) Sharp, K. W.; Koehler, W. H. *Inorg. Chem.* **1977**, *16*, 2258.
(37) Lyons, L. E.; Young, T. L. *Aust. J. Chem.* **1986**, *39*, 511.
(38) Raymond, C. C.; Dick, D. L.; Dorhout, P. K. *Inorg. Chem.* **1997**, *36*, 2678.
(39) Goldbach, A.; Johnson, J.; Meisel, D.; Curtiss, L. A.; Saboungi, M. L. *J. Am. Chem. Soc.* **1999**, *121*, 4461.
(40) Cusick, J.; Dance, I. *Polyhedron* **1991**, *10*, 2629.
(41) Hassoun, J.; Scrosati, B. *Adv. Mater.* **2010**, *22*, 5198.